Improved estimate of tidal dissipation within Mars from MOLA observations of the shadow of Phobos

Bruce G. Bills,[1,2] Gregory A. Neumann,[1,3] David E. Smith,[1] and Maria T. Zuber[1,3]

Received 4 November 2004; revised 4 January 2005; accepted 21 April 2005; published 26 July 2005.

[1] We report on new observations of the orbital position of Phobos, the innermost natural satellite of Mars, and show that these observations provide an improved estimate of the rate of tidal dissipation within Mars. The observations were made with the Mars Orbiter Laser Altimeter instrument on the Mars Global Surveyor spacecraft. The secular acceleration in along-track orbital motion is conventionally expressed in terms of a quadratic term in mean orbital longitude, which yields $s = (dn/dt)/2 = (136.7 \pm 0.6) \times 10^{-5}$ deg/yr^2, where n is the mean motion. The corresponding fractional rate of change in orbital angular velocity is $(dn/dt)/n = (6.631 \pm 0.029) \times 10^{-9}$/yr, the highest measured for any natural satellite in the solar system. The energy dissipation rate is (3.34 ± 0.01) MW. Because Phobos is so close to Mars, there are nonnegligible contributions to the tidal evolution from harmonic degrees 2, 3, and 4. However, the elastic tidal Love numbers are observationally constrained only at degree two. The observed acceleration is consistent with that for a homogeneous Maxwell viscoelastic model of Mars with effective viscosity of $(8.7 \pm 0.6) \times 10^{14}$ Pa s.

Citation: Bills, B. G., G. A. Neumann, D. E. Smith, and M. T. Zuber (2005), Improved estimate of tidal dissipation within Mars from MOLA observations of the shadow of Phobos, *J. Geophys. Res.*, *110*, E07004, doi:10.1029/2004JE002376.

1. Introduction

[2] The Mars Orbiter Laser Altimeter (MOLA) instrument on the Mars Global Surveyor spacecraft has observed 15 transits of the shadow of Phobos across the surface of Mars, and has directly measured the range to Phobos on one occasion. The observed positions of Phobos and its shadow are in good agreement with predictions from orbital motion models derived from observations made prior to 1990, with the notable exception that Phobos is gradually getting ahead of its predicted location. This effect makes the shadow appear at a given location earlier than predicted, and the discrepancy is growing by an amount which averages 0.8 s/yr. We model this effect, and interpret the required modification in the orbital model as implying a revision to the rate of tidal dissipation within Mars. It has long been understood that tides can be effective in transferring angular momentum from the spin of a planet to the orbit of a satellite, or vice versa, depending on whether the satellite is above or below the synchronous elevation, at which the satellite orbital period matches the planetary rotation period. The process was first examined in detail by *Darwin* [1911] and in the case of the Earth-Moon system there is a very clear signal, with the Earth's spin slowing down, such that the length of the day is increasing by (2.3 ± 0.1) ms per century [*Stephenson and Morrison*, 1995] and the size of the lunar orbit is increasing at a rate of (3.84 ± 0.07) cm/yr [*Dickey et al.*, 1994].

[3] In the case of Io, the innermost large satellite of Jupiter, tidal heating produces very significant volcanism on the satellite [*Peale et al.*, 1979; *Lopes-Gautier et al.*, 1999; *Peale*, 2003]. However, there are two important differences between Io and the Moon, both of which slow the orbital evolution of the former. The tides raised by Io on Jupiter are substantial, but because Jupiter is gaseous, the tides are very nearly in equilibrium and dissipate little energy. Also, because Io is locked in resonance with its neighbors Europa and Ganymede, the associated orbital evolution, per unit of transferred angular momentum, is reduced [*Yoder and Peale*, 1981; *Peale and Lee*, 2002] and despite nearly 400 years ($\sim$81,500 orbits) of careful observations, even the sign of the change in orbital motion is still in dispute [*Lieske*, 1987; *Aksnes and Franklin*, 2001].

[4] The best known case of rapid orbital evolution in the solar system is Phobos, innermost of the two natural satellites of Mars. From the time of its discovery by Asaph Hall on 16 August 1877 [*Hall*, 1878], the orbital motion of Phobos has been intensively studied by Earth-based observers and from spacecraft. Phobos is very close to Mars, at a mean distance of 9378 km, compared to 3394 km radius of Mars, and with an orbital period of only 7.65 hours, is well within the synchronous orbital distance. In the 127 years since discovery, Phobos has completed $\sim$145,500 orbits, equivalent to 705 years for Io, and 10,880 years for the Moon. In terms of orbits completed under careful observation, Phobos can arguably lay claim to being the best studied natural satellite in the solar system.

[1] NASA Goddard Space Flight Center, Greenbelt, Maryland, USA.
[2] Scripps Institution of Oceanography, La Jolla, California, USA.
[3] Massachusetts Institute of Technology, Cambridge, Massachusetts, USA.

Copyright 2005 by the American Geophysical Union.
0148-0227/05/2004JE002376$09.00

Table 1. Phobos and Deimos Secular Acceleration Estimates

Source	Phobos, 10^{-5} deg/yr^2	Deimos, 10^{-5} deg/yr^2
Sharpless [1945]	188 ± 17	−26.6 ± 16
Sinclair [1972]	96 ± 16	−6.3 ± 4.4
Sinclair [1989]	123.7 ± 1.7	−0.28 ± 0.79
Jones et al. [1989]	124.0 ± 1.7	−0.20 ± 0.80
Jacobson et al. [1989]	124.8 ± 1.8	−1.57 ± 0.81
This work	136.7 ± 0.6	

[5] As might be expected from proximity to Mars, the orbit of Phobos is experiencing a secular acceleration. Using the theory of *Woolard* [1944], *Sharpless* [1945] estimated an along-track acceleration of $(1.82 \pm 0.17) \times 10^{-3}$ deg/yr^2. Subsequent observations have refined the estimate and models generated in support of the Russian Phobos mission [*Sagdeev and Zakharov*, 1989; *Avensov et al.*, 1989; *Morley*, 1989] all give concordant estimates, as indicated in Table 1. Given the long time span of the observations, and relatively high accuracy of the models, it might be supposed that little additional progress would occur. Indeed, relatively few additional observations of Phobos have been made until quite recently.

[6] Our primary interest in these MOLA observations is that they can provide information about the interior of Mars. Previous estimates of secular acceleration of Phobos have been used to determine the tidal quality factor, or Q, of Mars. This parameter is a common means of expressing the relative rate of tidal dissipation and is defined as the maximum energy stored in the tide, divided by the energy dissipated per cycle. High values of Q correspond to low rates of dissipation, per unit forcing. For any damped oscillator system, the value of Q depends both on intrinsic properties of the oscillator, and upon the frequency of the oscillation and without further information, it is difficult to determine what the Q would be at other frequencies. For that reason, we will estimate an effective viscosity for Mars which yields the observed tidal effects. However, since much of the previous work on tidal dissipation within Mars, and other planets, has been formulated in terms of Q values, we will also use this formulation.

[7] On the basis of previous analyses of the orbital acceleration of Phobos, the tidal Q of Mars has been estimated to be $Q = (100 \pm 50)$ [*Smith and Born*, 1976; *Yoder*, 1982]. For comparison, the tidal Q of Jupiter is likely in excess of 10^6 [*Goldreich and Nicholson*, 1977; *Ioannou and Lindzen*, 1993] and that of Earth is ∼10. However, most of the dissipation of lunar tides occurs in the oceans [*Egbert and Ray*, 2003]. It has only recently been possible to remove the much larger oceanic dissipation and estimate the solid Earth tidal $Q = (280 \pm 70)$ [*Ray et al.*, 2001]. This is in agreement with damping of seismic normal modes [*Widmer et al.*, 1991]. It thus appears that Mars is more dissipative than Earth. This is an important conclusion, if true, and attempting to better understand this situation is part of our motivation for the current study.

[8] In an analysis of tidal dissipation within Mars, the secular acceleration of Deimos is also potentially informative. It is outside the synchronous orbital distance, and is thus expected to be evolving away from Mars. The astrometric observations of Deimos are nearly as numerous and accurate as those of Phobos, but the secular acceleration is small enough that the signal-to-noise ratio is not nearly as good for Deimos, as can be seen in Table 1. In contrast to the case for Phobos, where all of the recent estimates are in good agreement, there is still considerable scatter among the Deimos estimates.

2. Observations

[9] We will present and discuss three types of observations which constrain the orbital position of Phobos. The first set of observations are measurements of the distance to Phobos by the MOLA instrument on MGS. The second set comprise detections of the shadow of Phobos on the surface of Mars by MOLA. The earliest measurements we discuss are observations by the camera on the Viking I lander as the shadow of Phobos passed over it in 1977.

2.1. Range to Phobos

[10] The MOLA instrument was designed to measure the topography of Mars with a laser [*Zuber et al.*, 1992; *Abshire et al.*, 2000; *Smith et al.*, 2001a]. In that mode of operation, it transmitted a short (8 ns) pulse of laser light at 1064 nm wavelength, and detected the reflected pulse in a 50 cm aperture telescope, with 0.8 mrad field of view. The round-trip time of flight of the laser pulse determines the range from the spacecraft to the surface bounce point. The instrument time is related to the spacecraft clock with submillisecond precision [*Neumann et al.*, 2001], and spacecraft time is maintained by the Mars Global Surveyor project with accuracy better than 30 milliseconds relative to UTC. Onboard sensors determine the orientation of the spacecraft with an accuracy of ∼1 mrad, and radio tracking from Earth determines the trajectory of the spacecraft about Mars with an accuracy of a few meters. Thus MOLA provides an inherently precise and bias-free measurement of planetary radius and related events at Mars.

[11] The direct range measurement to Phobos was made on 12 September, 1998, during one of four close encounters between MGS and Phobos during the aerobraking mission phase. As discussed by *Banerdt and Neumann* [1999], a total of 627 range measurements were acquired, over a span of 63 s, and agreement between the measured range and previous estimates of Phobos surface topography were quite good, but required estimation of the location of the laser footprints on the surface of Phobos and a small correction to the satellite orbit. There was a 4 km discrepancy between the measured and estimated ranges, but with a total positional accuracy estimate for the model of 17 km, this was not seen as anomalous.

2.2. Shadow Detections

[12] The MOLA instrument is currently in use as a passive radiometer. It no longer fires its laser, since the master clock oscillator failed in 2001, halting the laser after 700 million pulses. However, its detector continues to sense the 1 micron brightness of the surface of Mars. The surface spot size depends on viewing geometry, but in nadir-pointed mode, the field of view is a circle with radius 300 m. In the passive radiometer mode, background brightness is integrated over 1/8 s intervals (1 s intervals during topographic mapping), during which time the detector ground track advances 375 m. The MOLA detector thus functions as a 1-pixel camera, with a roughly 300 × 500 m resolution, which is intermediate between that of imagers such as

Table 2. Phobos Shadow Events

Event	Identifier	Date	Time, UTC h:m:s	Duration, s	Offset, s	Error, s	E Longitude, deg	N Latitude, deg
a	VL1-263	1977 Sep 20	20:40:03.718	30	−16.	3.0	312.0434	22.2689
0	Flyby 551	1998 Sep 12	22:44:31.638	63	1.75	0.25	337.3135	23.7130
1	AP10758L	1999 May 10	23:07:40.975	25	2.0	2.0	73.8112	−35.4330
2	AP11211L	1999 Jun 16	15:44:29.745	20	1.4	0.2	176.7834	−18.7435
3	AP11994L	1999 Aug 19	11:11:57.587	15	1.7	0.2	138.0214	8.0011
4	AP12080L	1999 Aug 26	04:00:29.597	18	1.8	0.2	310.3241	10.5700
5	AP19166L	2001 Mar 27	06:11:53.914	35	2.8	0.2	98.3065	−38.7748
6	AP20266L	2001 Jun 25	05:35:29.846	15	3.2	0.2	251.3572	6.0409
7	AR02012B	2002 Jan 12	21:20:29.756	23	5.6	1.0	154.9400	47.9917
8	AR02118B	2002 Apr 28	04:19:45.634	15	5.7	2.5	347.9598	−0.6501
9	AR02151B	2002 May 31	01:00:16.445	18	4.7	0.5	355.1518	−13.6179
10	AR03092B	2003 Apr 02	15:32:22.254	20	6.7	0.2	211.7248	−14.0436
11	AR03356B	2003 Dec 22	12:31:21.916	19	5.1	0.2	277.7320	29.7939
12	AR04017B	2004 Jan 17	16:27:09.046	15	5.6	0.2	111.7624	17.6689
13	AR04069B	2004 Mar 09	16:35:19.534	16	4.8	0.2	252.0035	−1.0661
14	AR04124B	2004 May 03	21:14:38.725	17	3.3	2.0	355.2571	−20.3817
15	AR04180B	2004 Jun 28	01:50:29.156	47	4.6	2.0	100.2560	−49.2834

MOC, and the 3 × 5-km spots of the Thermal Emission Spectrometer.

[13] In radiometer mode, MOLA measures variations in albedo, changes in dust opacity, cloud cover, and seasonal variations in albedo of polar ice. The MGS extended mission phase has implemented a 16deg pitch to the spacecraft attitude so that the emission angle is no longer normal to the surface, with correspondingly greater uncertainty in the position and range to the MOLA footprint.

[14] The size of Phobos, and its distance from Mars, are such that the apex of the umbral cone, within which a total solar eclipse would be seen, does not reach the surface of Mars. The minimum diameter of the penumbra at the surface is ~60 km, when the shadow is located near solar nadir, but extends in a broad ellipse as the shadow marches from hemisphere to hemisphere with season. In any case, the passage of a shadow of Phobos through the MOLA field of view causes a detectable change in surface brightness.

[15] We searched the archive of surface brightness variations spanning three Mars years, concentrating on times when the predicted shadow centroid was within 50 km of the MOLA viewpoint. We have detected 15 shadow transits, with parameters listed in Table 2. The best shadow detections occur when the shadow is near the equator and is moving across low-relief, uniform albedo surfaces, but nearly all light curves have provided usable estimates of centroid time and duration of the darkening. Because solar brightness varies from center to limb and considerable light is scattered by atmospheric particles, the amount of darkening is not strictly proportional to, and is generally less than, the area of the solar disk obscured.

[16] In Table 2, we indicate for each detected shadow event the time and location of the centroid. We also list the estimated duration of the event, and an offset between the observed and computed centroid times. A positive offset means that Phobos was ahead of the estimate given by the *Jacobson et al.* [1989] ephemeris. We also list an error associated with the offset, which is determined by the least-squares fitting procedure, as described below.

[17] Under favorable circumstances, the observed "light curve" is quite analogous to what is seen when observing eclipsing binary stars through a telescope [*Wilson*, 1994]. Figure 1 illustrates one of the detected shadow events. It is listed as event 3 in Table 2, and has identifier AP11994L. The parameters of primary interest are the centroid time, and the duration and maximum amount of the darkening.

[18] The orbit of Phobos lies very nearly in the Mars equator plane, so the shadow motion is mainly in a longitudinal direction. The latitude of the shadow changes much more slowly, with one cycle per Mars year. As the subsolar latitude moves north after the vernal equinox, the shadow moves south of the equator. Since the obliquity of Mars is roughly 25.2 degrees and the orbital mean radius is 2.76 times the planetary radius, there are two periods during each Mars year during which the Phobos-Sun line fails to intersect the surface of Mars. The most recent shadow detection in Table 2 is the last one possible during the current eclipse season. For a more detailed discussion of the

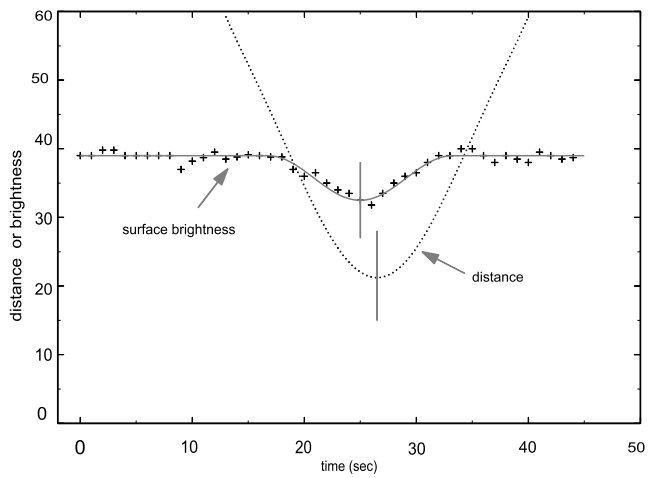

Figure 1. Shadow event detection. Plus signs indicate detected Mars surface brightness variations as seen by MOLA, as a function of time, for shadow event 3 in Table 2. The curve approximating the observations is computed via ray tracing, as explained in the text. Unit for radiance is $W/m^{-2}/sr/micron$. The other curve illustrates distance between the MOLA field of view and the predicted shadow centroid. The offset of 1.7 s between the minima of these two curves yields an estimate of the along-track correction, or the amount by which Phobos is ahead of schedule. Unit of distance is km.

Figure 2. Simulated solar views. Using the algorithm described in the text, simulated views of the partially eclipsed Sun are constructed at 1 s intervals for event 3 in Table 2.

spatial and temporal pattern of motion of the shadow, see *Bills and Comstock* [2005].

[19] The MGS spacecraft orbital inclination is 92.9 degrees, so its motion is mainly in a latitudinal direction. Both orbits (MGS and Phobos) have low eccentricities, and thus nearly uniform speed in the along-track direction. The shadow of Phobos is nearly circular when it is close to the subsolar point, and as it moves away from that point becomes elongated along the axis connecting the shadow centroid to the subsolar point. For small departures from the subsolar point, the shadow is approximately elliptical. When far from the subsolar point it departs somewhat from the elliptical form, since it is defined by the intersection of a nearly circular cone with a sphere. When circular, the shadow diameter is roughly 30 km. Due to the low inclination of the orbit, these circular shadows only occur near to the equinoxes. The duration of a shadow detection event depends on several parameters, including the size, shape, and orientation of the shadow itself, and how closely the MOLA field of view trajectory passes to the shadow centroid.

[20] To predict the light curve, rays are traced from the solar disk to the surface observation point during a window of time of approximately 45–60 s duration. We model the solar disk as an array of 70 × 70 pixels, each of them 20,000 km on a side, with a brightness that depends on wavelength and on the pixel's angular distance from center θ as μ^{α}, where $\mu = \cos(\theta)$ and $\alpha = 0.25$ at 1064 nm [*Hestroffer and Magnan*, 1998].

[21] We determine the position of the Sun and Phobos in Mars-centered, inertial (J2000) coordinates using the NAIF toolkit [*Acton*, 1996] applied to the nominal ephemeris kernel mar033-7 [*Jacobson et al.*, 1989; *Sinclair*, 1989], using the JPL Developmental Ephemeris DE410 [*Standish et al.*, 1995, 2003], correcting the position of the Sun for light-time and stellar aberrations. The rotations of Mars and Phobos are calculated according to the IAU2000 planetary model [*Seidelmann et al.*, 2002].

[22] The solar disk is eclipsed where a ray intersects the volume of Phobos, modeled as a triaxial ellipsoid with radii 13.4, 11.2, and 9.3 km. The normalized light curve is compared to the observations in a least-squares sense, where the model includes an unknown scale factor and background constant to account for attenuated and scattered light. A total of 45 s of time is modeled to establish a baseline. Figure 2 illustrates a sequence of simulated views of the partially eclipsed Sun, at 1 s intervals, as would be seen at points along the MOLA ground track for the same event as in Figure 1. In this case, the shadow center is 20 km off the MOLA track at closest approach, and the shadow intersects the field of view for only 15 s. Variations in surface albedo and illumination geometry are not accounted for in our model.

[23] The residual between observations and model can be minimized by adjusting the along-track position of Phobos with respect to the nominal ephemeris. The position in a direction perpendicular to the line of sight to the Sun, and to the along-track direction, may also be adjusted, while variations in the line of sight direction have virtually no effect.

[24] For a given shadow configuration, and MOLA ground spot trajectory, there will generally be two different along-track positions of Phobos that would yield nearly identical light curves. They are symmetrically placed on opposite sides of the position which would yield a profile across the center of the shadow. We have consistently reported the smaller of the two corrections to along-track position required to match the observed light curve. Figure 3 illustrates the pattern of misfit between observations and

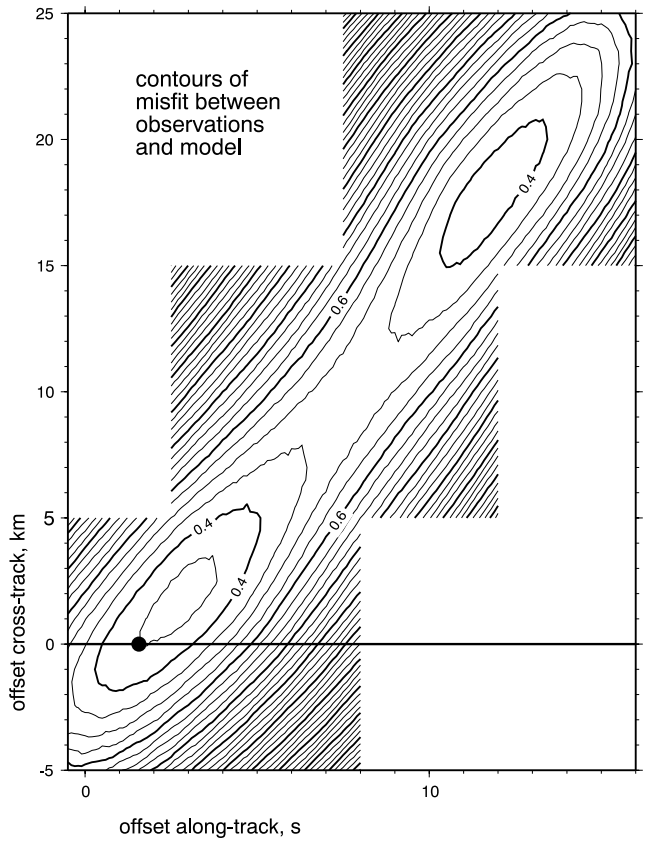

Figure 3. Misfit between MOLA observation and Phobos predicted position. Contours indicate variance of the misfit between observed brightness variations and computed brightness variations, as the trajectory of Phobos is perturbed away from that predicted by the *Jacobson et al.* [1989] ephemeris. Along-track perturbations are indicated in equivalent time, and cross-track perturbations are indicated in distance at the surface of Mars. Note that there are two broad minima, as discussed in the text. Dot indicates location of minimum misfit at zero cross-track perturbation.

Table 3. Phobos Astrometric Parameters

Event	Centroid Time, s From J2000	X, km	Y, km	Z, km	R.A., deg	DEC, deg	Radius, km	Distance, km
a	−703091948.10	−3094.292	−8594.233	−2423.227	250.19895	−14.85768	9450.266	19.130
0	−41087665.06	−8054.643	−3536.339	2859.596	203.70357	18.00800	9249.879	443.738
1	−20350275.84	4892.861	7860.377	1482.607	58.09891	9.09750	9376.765	24.765
2	−17180065.07	2252.691	8520.991	3227.711	75.19153	20.11343	9386.161	10.470
3	−11666808.23	−2528.991	7449.935	5139.557	108.75054	33.15520	9397.466	21.784
4	−11087906.220	−3029.349	7177.711	5257.641	112.88215	34.01356	9398.897	20.764
5	38945579.110	5030.245	7940.990	1375.630	57.64766	8.32565	9500.266	5.524
6	46719396.030	−1623.827	7864.463	5092.268	101.66629	32.37990	9508.827	14.600
7	64142495.190	−6640.438	−6812.832	138.236	225.73416	0.83246	9514.684	7.431
8	73239651.067	993.184	−8282.858	−4560.795	276.83760	−28.66606	9507.524	14.025
9	76078883.131	3215.532	−7230.846	−5267.656	293.97455	−33.64962	9506.470	6.685
10	102569607.690	1305.351	8609.128	3761.189	81.37825	23.36178	9485.124	7.448
11	125368348.600	−5025.887	−7830.112	−1378.661	237.30495	−8.42844	9405.897	4.637
12	127628894.480	−3102.292	−8448.254	−2706.365	249.83621	−16.73668	9397.958	18.383
13	132122184.970	749.179	−8181.034	−4545.936	275.23227	−28.95805	9389.149	8.932
14	136890945.410	4322.490	−6309.931	−5440.339	304.41230	−35.42414	9385.970	14.603
15	141659494.590	6797.421	−3565.760	−5406.967	332.31960	−35.16115	9389.082	8.591

predictions for the same event that was used in the previous figures.

[25] In all but two cases the minimum misfit position lies within 4 km of the nominal Phobos orbital plane. We do not consider the minimization in the cross-track direction to be sufficiently informative, pending a better understanding of the possible atmospheric effects on the shadow. Therefore we apply only the along-track perturbation in our analysis. Where the surface is reasonably uniform and the light curve is well-modeled, the precision of the estimate approaches 0.2 s, whereas in other cases the time and duration of the transit is less well resolved. Error estimates are therefore based on the discrepancy between the modeled perturbation with across-track shift constrained and unconstrained.

[26] Table 3 lists the derived position information for Phobos. We list both the time of each event and the corresponding position of Phobos. The positions are listed in Cartesian Mars-centered coordinates (X, Y, Z), and in terms of a distance and direction from the center of Mars. The direction is given in terms of right ascension and declination in the J2000 system. We also list the distance of the shadow center from the MOLA ground track, at the time of closest approach.

[27] We also searched for Deimos shadow events and did not find any. Because Deimos is both smaller and farther from the surface of Mars, the shadows would be much fainter. There were three occasions when the MOLA field of view passed through the estimated location of a Deimos shadow, but the background albedo variations are too high to allow a secure detection.

2.3. Viking Lander Transits

[28] We also revisit the transits of Phobos seen by the Viking lander 1 in 1977 [*Duxbury*, 1978; *Christou*, 2002]. These data are archived in the Planetary Data System (PDS) Geosciences Node. Three images were taken during transits with the scan platform held fixed on 20, 24, and 28 September 1977. The first of these images (11F119 on DOY 263) showed a darkening of the ground in the red, green and blue filters, with sky slightly darkened but most of the time saturated. Local time of this image was early afternoon (14.11h) so that scattered light was minimal. Local times here are reported in Mars equivalent hours, which are 1/24 of a Mars mean solar day, and are thus roughly 1.0275 terrestrial hours in duration [*Allison and McEwen*, 2000].

[29] The second and third images (12F125 and 12F136) show darkening of ground and sky and were taken at local times of 16.87 and 17.80. The predicted path of Phobos' shadow center approached within 20 km on the 20th and 28th, while on the 24th, the closest approach was more than 65 km away and it is likely that all of the darkening was from skylight. The atmosphere was dusty at the time, making the effect of the shadows in late afternoon difficult to model in a straightforward fashion.

[30] We have averaged the DNs of ground pixels (1–430) for the first transit and show the light curves on the three filters in Figure 4. The coordinates of the lander were established by radiometric tracking [*Folkner et al.*, 1997], given in the IAU1994 reference frame. Translated to the IAU2000 planetocentric coordinate system, the Lander's

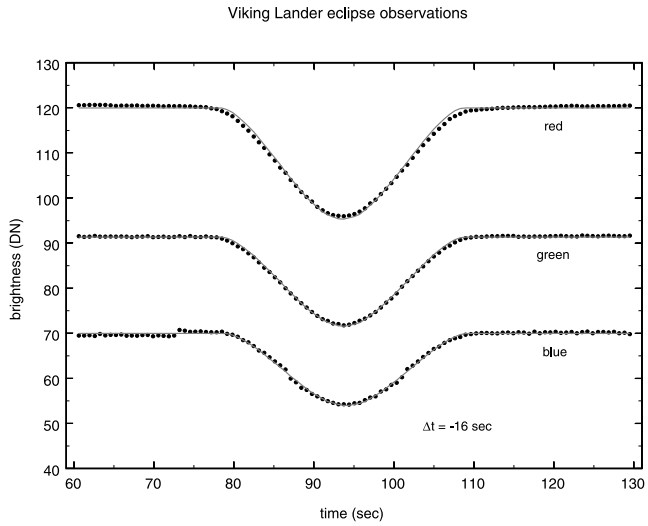

Figure 4. Viking Lander shadow observations. Observed brightness variations in red, green, and blue channels, for shadow event on 20 September 1977, are compared with computed variations using model procedure described in text.

coordinates are 312.04343deg E, 22.26891deg N, at radius 3389.3156 km.

[31] The start time of the image recording is given in the PDS label, but the stop time is approximate. The transit lies mid-image, so that timing depends on the line rate assumed. *Christou* [2002] inferred the scan time on the basis of the number of sample bits 3072 plus a variable number of engineering bits. This was assumed to be 3414 for each of three colors, which was divided by telemetry rate (16000 bps) to give 0.640125 s. The camera was designed to scan in increments of 0.12deg, with a scan rate of 5.52 scans per degree [*Patterson et al.*, 1977]. Using these parameters we obtain a scan time of 0.6624 s, slightly longer than that used by the PDS to calculate end time. *Christou* [2002], using a spherical shadow approximation, obtained an offset for this transit of −10 s, while we estimate it at −16 s. Using the image duration inferred from telemetry rates, we would infer an offset of −13 s. Although the image start time is thought to be accurate to 1 s, an uncertainty of 3 s in transit offset time must be assumed.

[32] We also note that there have been recent observations of both Phobos and Deimos from the PanCam instruments on the Mars Exploration Rovers [*Bell et al.*, 2004a, 2004b]. We have not included these observations in our current analysis for three reasons. First, they overlap in time with the MOLA observations, and thus provide less information on purely secular effects than would be the case for earlier or later observations. Second, they have not yet been reduced to astrometric form. Third, the time at which the observations were made is difficult to reconstruct at the required accuracy, since the rover onboard clock was never intended for such precise applications. However, we do anticipate that these observations will be useful in constraining future ephemeris studies of both Phobos and Deimos.

3. Fit to Observations

[33] We now describe our analysis of the recent observations, and explain the changes required in the orbital model to accommodate both the MOLA observations and the previously collected ground-based and spacecraft observations. As additional observations accumulate, both from MOLA and from other orbiting and landed instruments at Mars, it will likely become necessary to perform a complete new analysis. This is partly due to the fact that spacecraft observations have provided significantly improved estimates of the gravitation field [*Lemoine et al.*, 2001; *Yuan et al.*, 2001] and rotational parameters [*Folkner et al.*, 1997] of Mars, and thus the gravitational forcing experienced by Phobos is considerably better understood than was the case in 1990.

[34] However, as the corrections required to fit the new observations are very small, and appear to be almost entirely along-track perturbations, we can use a very simple linear perturbation analysis and adjust only 3 parameters. If the adjustments in time of along-track position were large, compared to the shortest forcing periods, this simple linearization would not be sufficient. The orbital model has secular effects, long period effects, and short period effects, and the forcing periods are mainly at harmonics of the Mars heliocentric orbital period, and the Phobos mean orbital period. As these periods are incommensurate, the orbital motion is quasi-periodic and a shift in time by a significant fraction of the shortest period will alter the structure of the beat patterns between the input periods. However, the rate of accumulation of along-track position error is equivalent to 0.8 s/yr, or a few parts in 10^7, and the linear analysis is warranted.

[35] The parameters we adjust are only those which determine the unperturbed orbital mean longitude. That is, we write

$$\lambda(t) = L + n(t-\tau) + s(t-\tau)^2, \tag{1}$$

where λ is the mean longitude, L is the mean longitude at the reference epoch τ, the mean motion is n, and s is a term related to secular acceleration. Note that the secular acceleration in longitude, or rate of change of mean motion, is

$$\frac{dn}{dt} = 2s(t-\tau). \tag{2}$$

It could thus be argued that $2s$ would be a better parameter to estimate. However, the form listed above is quite traditional, in the literature on Phobos and Deimos, and we retain it here. However, in comparing estimates of secular acceleration for other satellites, caution is required, as the parameterization scheme varies.

[36] A common means of illustrating the effect of the secular acceleration, apparently initiated by *Sharpless* [1945], is to fit a model which includes secular acceleration to the observations, and then suppress the acceleration term. A plot of the mean longitude residuals of the observations, as a function of observation time, should be mainly parabolic in form. When Sharpless first utilized the display, a parabolic trend was evident, but fairly significant periodic residuals were also present. As the models and observations have improved with time, and the time span itself has increased, the parabolic trend has become dominant, as is seen in Figure 5a. The longitude residuals from the observations prior to 1990 are taken from *Jones et al.* [1989]. The MOLA points are clearly separated in time from the rest and have errors too small to be seen at this scale. An expanded view is given in Figure 5b.

[37] Our initial estimates of the parameters L, n, and s are from *Jacobson et al.* [1989]:

$$\begin{aligned} L &= (138.003 \pm 0.026)\ \text{deg}, \\ n &= (1128.8444070 \pm 0.0000020)\ \text{deg/d}, \\ s &= (1.249 \pm 0.018) \times 10^{-3}\ \text{deg/yr}^2. \end{aligned} \tag{3}$$

Our adjusted estimates, obtained from a least-squares fit to the augmented data set, are

$$\begin{aligned} L &= (137.790 \pm 0.015)\text{deg}, \\ n &= (1128.8444068 \pm 0.0000013)\text{deg/d}, \\ s &= (1.367 \pm 0.006) \times 10^{-3}\ \text{deg/yr}^2. \end{aligned} \tag{4}$$

In both cases, the stated errors reflect one standard deviation. We compare our estimate of the secular

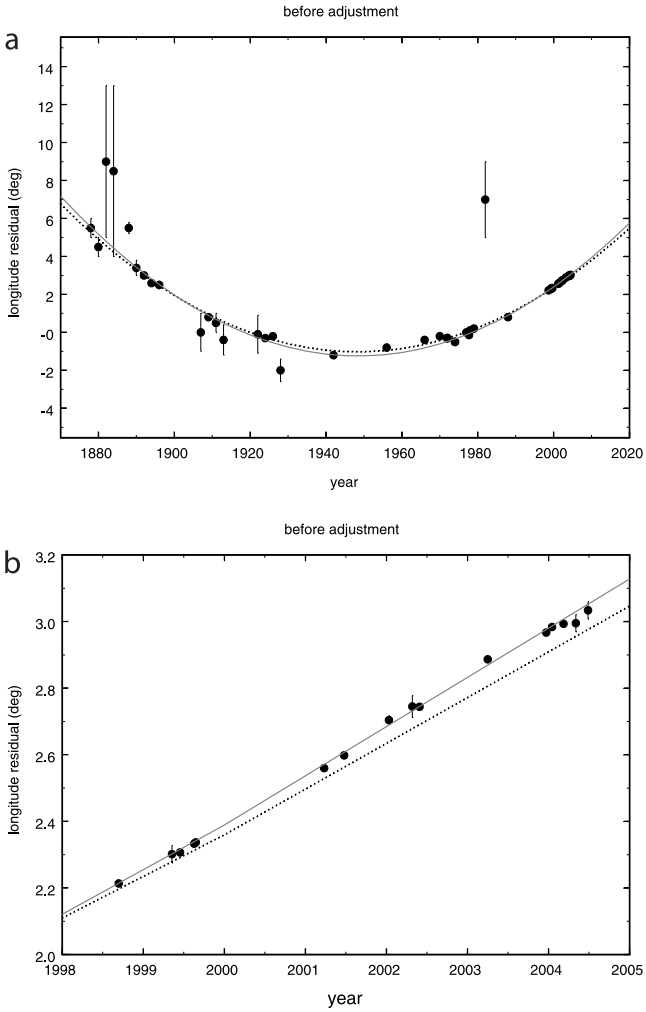

Figure 5. Phobos longitude residuals. Circles indicate mean difference between observed orbital longitude of Phobos and that predicted by the *Jacobson et al.* [1989] model when the secular acceleration term is set to zero. Each of the curves is a parabola fit to the residuals, one without, and the other with, the MOLA observations. (a) Full range of residuals. (b) Expanded view of recent results.

acceleration term with several previous estimates in Table 1. Residuals with respect to the new estimates are shown in Figure 6. Note that the parameters L and n are dependent upon the reference epoch τ, but the curvature of the residuals, which is determined entirely by the parameter s, is invariant to epoch shifts. As an example, the change in mean motion in our adjustment was very small, and with a change in epoch, we could have made it zero. The least-squares adjustment process also yields error estimates for the adjusted parameters. Note that the relatively few MOLA observations have reduced the error in the estimate of the parameters quite substantially. That is due, in part, to the higher accuracy compared to earlier observations, and partly due to the extended time baseline. The interval between the latest MOLA observation and the 1988 opposition, at which the most recent observations used in previous analyses were collected, is 14% of the complete time span from the discovery of Phobos.

[38] Another point of interest is that our estimate of the secular acceleration rate differs from the previous estimate by 6 times the standard error of the previous estimate. The Phobos ephemeris of *Jacobson et al.* [1989] was based on the best estimates of the gravity field and rotational parameters of Mars available at that time. Subsequent work has dramatically improved knowledge in both those areas [*Yuan et al.*, 2001; *Folkner et al.*, 1997] and it seems that the time is right for a full new analysis of the orbits of Phobos and Deimos. The upcoming Mars Express close encounters with Phobos will provide additional important constraints.

4. Interpretation

[39] We now turn to an interpretation of the secular acceleration in the orbit of Phobos. The change in secular acceleration required to fit the MOLA observations is quite small. However, we use this occasion to revisit the connection between orbital effects and internal causes. Past analyses concerned with long term evolution of the satellite orbit [*Burns*, 1972, 1992; *Lambeck*, 1979; *Cazenave et al.*,

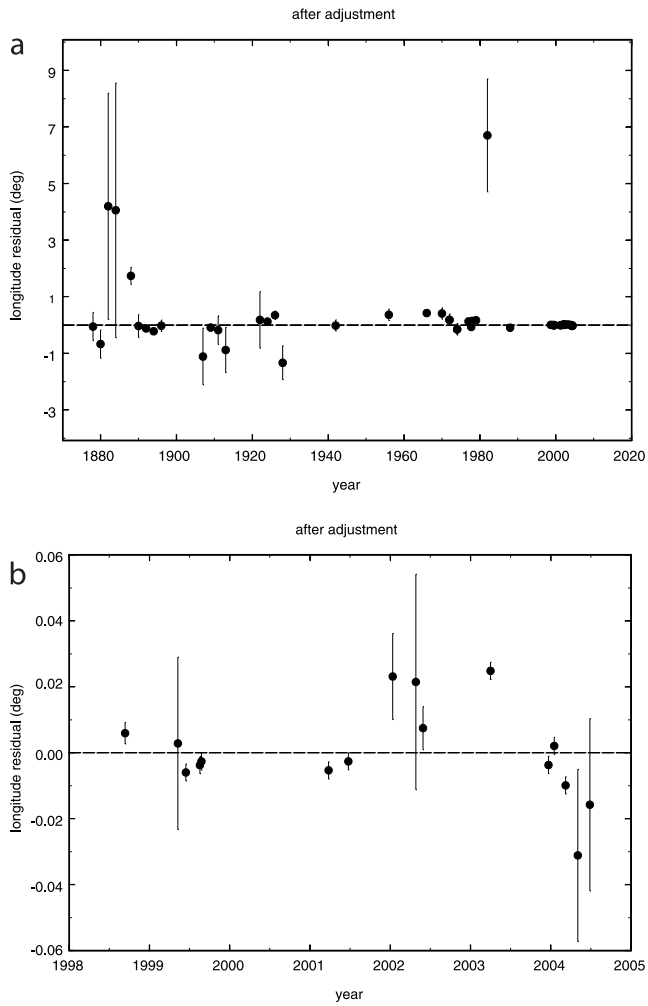

Figure 6. Phobos longitude residuals. Similar to Figure 5, but in this case the computed longitude includes the parabolic trend estimated by fitting to all of the observations. (a) Full range of residuals. (b) Expanded view of recent results.

1980; *Mignard*, 1981; *Yoder*, 1982; *Szeto*, 1983; *Yokoyama*, 2002] have consistently assumed that the observed acceleration arises from tidal dissipation within Mars, rather than from interaction with the solar wind [*Russell et al.*, 1990; *Sauer et al.*, 1995; *Mordovskaya et al.*, 2001], the dust torus [*Hamilton*, 1996; *Nazzario and Hyde*, 1997; *Howard et al.*, 2003], or other possible dissipative effects. *Yoder* [1982] has raised the issue of dissipation within Phobos. In the present study we assume that the dominant effect is due to tidal energy dissipation within Mars, and attempt to quantify that process.

[40] We will consider four elements of the tidal process. The response of an ideal elastic body to tidal perturbations sets much of the required background. We then consider the influence on the orbit of a delay in tidal deformation, which causes the tidal bulge to be misaligned with the tide raising body. Next we consider the behavior under tidal forcing of a particular model of viscoelastic deformation. Finally, we consider the long term orbital evolution of a pair of tidally interacting bodies.

[41] If the tide raised by Phobos on Mars were in equilibrium with the tide raising potential, there would be no influence on the orbit. However, if there is a delay or time lag between the cause and effect, then the tidal bulge applies a torque on the satellite and angular momentum is exchanged between the spin of Mars and the orbit of Phobos. The torque is proportional to the amplitude of the tide and to the sine of the lag angle. The basic assumption of our tidal analysis is that Mars responds linearly to imposed gravitational potentials. An imposed potential Φ will cause the body of Mars to deform, and thus give rise to an induced potential Ψ. If the potentials are expanded in terms of spherical harmonics, we can write

$$\Psi_j(r,\theta,\phi) = k_j \Phi_j(r,\theta,\phi), \tag{5}$$

where $\{r, \theta, \phi\}$ are the spherical coordinates of a point near Mars, j is the harmonic degree, and k_j is a proportionality constant, or Love number [*Love*, 1911; *Munk and MacDonald*, 1960]. The Love numbers depend on internal structure of the deforming body, and reflect a competition between elastic and gravitational influences. If the elastic rigidity is sufficient, the body will deform very little, and the Love numbers will be near zero. If the gravitational effect dominates, the response will be purely hydrostatic. For a purely elastic body, the induced potential will be exactly aligned with the imposed potential, and there will be no torque, no dissipation, and no influence on the orbit. If there is dissipation, as would occur in a viscous or viscoelastic body, then the deformation will lag behind the imposed potential. The rate of energy dissipation is proportional to the product of the stress times the strain rate, and will depend on the density, rigidity, viscosity, and rate of periodic forcing.

4.1. Elastic Models of Tidal Deformation

[42] For homogeneous elastic bodies, with density ρ and rigidity μ, the tidal Love numbers have values [*Munk and MacDonald*, 1960]

$$k_j = \frac{3}{2(j-1)}\left(\frac{\xi}{\xi + \mu w_j}\right), \tag{6}$$

where the effective gravitational rigidity is

$$\xi = \rho g R, \tag{7}$$

the surface value of gravity is

$$g = \frac{4\pi G}{3}\rho R, \tag{8}$$

and a numerical factor, different for each harmonic degree, is

$$w_j = \frac{2j^2 + 4j + 3}{j}. \tag{9}$$

The effective gravitational rigidity of Mars is

$$\xi = 49.68 \text{ GPa}. \tag{10}$$

If we assume a value for the elastic rigidity of

$$\mu = 100 \text{ GPa}, \tag{11}$$

which is typical of Earth's upper mantle [*Dziewonski and Anderson*, 1981], we obtain estimates of the Love numbers

$$k_2 = 0.0745,$$
$$k_3 = 0.0324, \tag{12}$$
$$k_4 = 0.0188.$$

Recent estimates of the degree 2 Love number of Mars derived from tracking of the Mars Global Surveyor (MGS) orbiter are given in Table 4. The measurement of k_2 is difficult, for numerous reasons [cf. *Smith et al.*, 2003]. First, the effect is small. Second, variations in the line-of-sight geometry from Earth to Mars change the observability of the effect over the course of a Mars synodic year. Third, current orbiters are in Sun-synchronous orbits implying that the spacecraft orbit is seeing the same nearly constant phase of the tide. For MGS, at about 2:00 PM local time, the spacecraft is principally sensitive to the latitudinal tidal component as the Sun's subsolar point moves in latitude through the Mars seasons. Finally, there are temporally correlated variations in the gravity field of Mars, associated with seasonal mass flux into and out of the polar regions [*Smith et al.*, 1999]. These temporal variations in low degree terms of the spherical harmonic representation of the gravity field produce perturbations of spacecraft in orbits such as MGS that are comparable in magnitude to the tidal perturbations [*Smith et al.*, 2001b].

[43] In practice, the recovery of k_2 is accomplished in concert with other Mars dynamical parameters. Given the small amplitude of the signal and the number of parameters being solved for, it has been common to simplify the representation of the tidal potential by assuming symmetry about the subsolar point. In this formulation the amplitude of deformation is dependent only on the angular distance from the subsolar position and is represented by a set of zonal coefficients (k_2,k_3, ...), of which the term with the greatest power is the degree 2 term. This simplification

Table 4. Estimates for k_2 Love Number

Parameter	Value	Source	Solution
k_2	0.055 ± 0.008	*Smith et al.* [2001b]	all data, weighted
k_2	0.195 ± 0.003	*Lemoine et al.* [2001]	all data, weighted
k_2	0.201 ± 0.059	this paper	all data, weighted
k_2	0.163 ± 0.056	this paper	best data
$k_{2,2}$	0.153 ± 0.017	*Yoder et al.* [2003]	best data

implies that asymmetric components of the potential equal the symmetric component (i.e., $k_2 = k_{2,0} = k_{2,1} = k_{2,2}$). In their recovery of the tidal potential, *Yoder et al.* [2003] instead implemented the more general form of the potential and solved for $k_{2,2}$, citing the fact that this term produced a secular drift in the orbital inclination of a spacecraft in the Sun-synchronous configuration. Their recovery was only possible because the eccentricity of the MGS orbit caused the spacecraft local time to drift slightly from Sun synchronous.

[44] Another factor contributing to the quality of Love number estimates is the solution methodology, i.e., what parameters are adjusted or modeled in the inversion of the tracking data. Spacecraft orbital geometry is mainly constrained by tracking from Earth and sensitivity to tidal effects varies as the orbit plane orientation changes relative to the Earth-Mars line. Use of data acquired in the most favorable observing periods is thus crucial to obtaining a well-constrained estimate.

[45] The lowest of the k_2 estimates in Table 4 is in good agreement with the prediction above, from a homogeneous model. Subsequent determinations produced larger values, with the best-determined values using only the data when the MGS spacecraft was in a desirable viewing geometry with respect to Earth. These larger values (0.153–0.163) could be matched either by taking an effective elastic rigidity of roughly 50 GPa, or by assuming a weak region in the interior, such as a fluid core. Elastic Love numbers of nonhomogeneous bodies can be computed via algorithms given by *Alterman et al.* [1959], *Peltier* [1974], and *Wilhelm* [1986].

4.2. Tidal Phase Lag

[46] *Redmond and Fish* [1964] presented an analysis of the secular acceleration, due to tidal dissipation, of a body in a nearly circular orbit. Their analysis considered tides of harmonic degrees 2 and 3, and equated the change in orbital angular momentum to the applied gravitational torque. It is easily generalized to yield

$$\frac{1}{n}\frac{dn}{dt} = -3n\alpha \sum_{j=2} k_j F_j(\gamma) \left(\frac{R}{a}\right)^{2j+1}, \tag{13}$$

with R the planetary radius, a the orbital semimajor axis, and

$$F_j(\gamma) = \frac{dP_j(\cos\gamma)}{d\gamma} \tag{14}$$

$$\alpha = \frac{m_s}{m_p}, \tag{15}$$

where $P_j[x]$ is a Legendre polynomial of degree j, m_s and m_p are the masses of the satellite and primary respectively, and γ is the tidal lag angle, or angular separation between imposed and induced potentials associated with harmonic degree j. If the dissipation is strongly dependent on forcing frequency, the lag angles at different harmonic degrees will be somewhat different. The first few angular coefficients in the series are

$$F_2(\gamma) = -\frac{3}{2}\sin 2\gamma \simeq -3\gamma, \tag{16}$$

$$F_3(\gamma) = -\frac{3}{8}(\sin\gamma + 5\sin 3\gamma) \simeq -6\gamma, \tag{17}$$

$$F_4(\gamma) = -\frac{5}{16}(2\sin 2\gamma + 7\sin 4\gamma) \simeq -10\gamma. \tag{18}$$

[47] A difficulty in estimating the tidal lag angle is that the observed orbital motion depends on several other parameters, whose values are not particularly well known. *Smith and Born* [1976] used this model, truncated at degree $n = 3$, in their analysis of tidal dissipation in Mars. They faced the problem that the mass of Phobos was not well known at that time. Subsequent estimates have much improved the situation, and we adopt the estimates [*Yuan et al.*, 2001] for Phobos, Deimos, and Mars

$$G\,m_{s1} = (7.14 \pm 0.19) \times 10^{-4}\,\mathrm{km^3 s^{-2}}, \tag{19}$$

$$G\,m_{s2} = (1.50 \pm 0.11) \times 10^{-4}\,\mathrm{km^3 s^{-2}}, \tag{20}$$

$$G\,m_p = (42828.382 \pm 0.001)\,\mathrm{km^3 s^{-2}} \tag{21}$$

so that the factors of interest here, the ratios of the satellite and planet masses, are

$$\alpha_1 = (16.67 \pm 0.43) \times 10^{-9}, \tag{22}$$

$$\alpha_2 = (3.50 \pm 0.25) \times 10^{-9}, \tag{23}$$

with virtually all of the error coming from the Phobos and Deimos mass estimates.

[48] A remaining problem in estimating the tidal phase lag is that the higher degree Love numbers are completely unconstrained by direct observations. If we take the uniform density, elastic body values listed above as estimates of the relevant Love numbers, and assume that the phase lag is the same for all harmonic degrees, we can write

$$\frac{1}{n}\frac{dn}{dt} = \alpha\,\gamma\,n\,(4186 + 478 + 60 + 8) \times 10^{-6}, \tag{24}$$

where the separate contributions from harmonic degrees 2, 3, 4, and 5 are listed. Using this relation, we find that the apparent tidal lag angle is

$$\gamma = (0.6694 \pm 0.0029)^\circ, \tag{25}$$

and the corresponding tidal quality factor is

$$Q = 1/\tan\gamma = 85.58 \pm 0.37. \quad (26)$$

It should be noted that the quoted error is a formal estimate only, and does not take into account the considerable uncertainty in the elastic Love numbers nor the possible variation in phase lag with harmonic degree. In fact, in the following section, we will see that the phase lags are likely to be quite different.

4.3. Viscoelastic Deformation

[49] We now attempt to relate the tidal phase lag to physical processes within Mars. The simplest example of a rheological model in which the tide would lag behind the imposed potential is a Maxwell viscoelastic structure, which is effectively a series connection of elastic and viscous elements. Maxwell viscoelastic models of the Earth are often used in consideration of postglacial rebound [*Peltier*, 1974; *Vermeersen and Sabadini*, 1997] and associated rotational perturbations [*Sabadini and Peltier*, 1981; *Sabadini et al.*, 1993]. In many discussions of planetary tidal dissipation [*Segatz et al.*, 1988; *Peale*, 2003], and associated orbital evolution [*Fischer and Spohn*, 1990; *Hussman and Spohn*, 2004], Maxwell rheology is also invoked. A limitation of these previous analyses, in the present context, is that the tidal potential has been limited to the lowest order (degree j = 2) terms, as is appropriate for more distant planet-satellite interactions. However, for consideration of the Mars-Phobos interaction, we are obligated to include higher order terms. In order to make our analysis more transparent and easily extensible, we will briefly review some of the fundamentals.

[50] The elastic element of a Maxwell viscoelastic structure, in which stress is proportional to strain, is characterized by a rigidity μ. The viscous element, in which stress is proportional to strain rate, is characterized by a viscosity η. For a series connection of these elements, the stresses within them are equal and the strains are additive. In response to a step-loading event, a Maxwell body will exhibit an initial elastic strain, followed a steady viscous strain rate. The Maxwell relaxation time

$$\tau = \frac{\eta}{\mu} \quad (27)$$

is the time required for the viscous strain to equal the initial elastic strain.

[51] In response to a periodic forcing, with frequency ω, a Maxwell body will have stress

$$\sigma(t) = S\exp(i\ \omega\ t) \quad (28)$$

and strain

$$\varepsilon(t) = E\exp(i\ \omega\ t). \quad (29)$$

The stress and strain functions can be related to each other via an effective modulus, as though they were elastic:

$$S = \mu^*(\omega)\ E. \quad (30)$$

The primary departure from a pure elastic response is that the effective rigidity is complex and frequency dependent. It can be written as

$$\mu^*(\omega) = \mu\left(\frac{(\omega\tau)^2 + i\ \omega\tau}{1 + (\omega\tau)^2}\right). \quad (31)$$

The real part represents the component of response which is in phase with the forcing, and the imaginary part is the response in quadrature. At high frequencies ($\tau\ \omega \gg 1$) the response is mainly elastic and is very nearly in phase with the forcing. At low frequencies, it is mainly viscous and will lag behind the forcing by amounts approaching 180°.

[52] The tidal response of a homogeneous Maxwell body is obtained via substitution of the effective modulus (31) into the formula for the tidal Love number for an elastic body (6). Because the tidal response has both buoyant and viscoelastic components, and they are effectively connected in parallel, the phase behavior is somewhat different than for a purely viscoelastic element. The response is nearly in phase with the forcing at both high frequencies, where the response is effectively elastic, and at low frequencies, where the response is mainly that of a buoyant fluid. Only at intermediate forcing periods is there any appreciable phase lag χ, and it is obviously a function of the forcing frequency. The maximum phase lag for a homogeneous Maxwell body occurs at frequencies ω for which

$$\tau^2\omega^2 = \frac{\xi}{\xi + w_j\,\mu} \quad (32)$$

and has a value

$$\chi_{\max} = \tan^{-1}\left(\frac{w_j\,\mu}{2\sqrt{\xi(\xi + w_j\,\mu)}}\right) \quad (33)$$

which is independent of viscosity. At forcing frequencies which are either higher or lower than this value, the phase lag will be less. This phase lag is very important for the secular orbital evolution problem. If the tidal bulge raised on Mars by Phobos were exactly aligned with the current position of Phobos, there would be no tidal torque.

[53] Note that the variations with forcing frequency in the real and imaginary parts of the forced response are quite different. The real part is essentially independent of frequency on the high frequency part of the curve, where the elastic aspect is dominant, and has a +2 logarithmic slope on the low frequency part of the curve, where viscous flow dominates. The imaginary part of the Love number has somewhat similar low frequency behavior, but with a +1 logarithmic slope, and at high frequencies, rather than being independent of frequency, it is has a −1 logarithmic slope. The maximum value of the imaginary part of the Love number occurs at the frequencies for which

$$\tau^2\omega^2 = \left(\frac{\xi}{\xi + w_j\,\mu}\right)^2, \quad (34)$$

Table 5. Tidal Forcing Periods

Body	Sidereal Rate, deg/d	Synodic Rate, deg/d	Synodic Period, hours
Sun	0.524	−350.368	24.660
Phobos	1128.844	777.952	11.106
Deimos	285.162	−65.730	131.447

which is similar to, but somewhat different than, the criterion for maximum phase lag, as discussed immediately above.

[54] The absolute value of the tidal Love number is the quantity reported in Table 4. For a homogeneous Maxwell body, it can be written as

$$|k_j| = \frac{3}{2(j-1)} \sqrt{\frac{\xi^2(1+\tau^2\omega^2)}{\xi^2 + \left(\xi + \mu w_j\right)^2 \tau^2 \omega^2}}. \tag{35}$$

[55] In a layered viscoelastic body, the response will be more complicated, but can still be described by a summation over the individual responses of the normal modes of the body [*Wu and Peltier*, 1982; *Vermeersen et al.*, 1996]. Each of the modal responses is identical in form to that for a homogeneous body; all that changes is the amplitude and relaxation time. That is, each mode contributes a real response which has the same structure as the homogeneous body's real response, but with a different amplitude and peak forcing frequency. The same is true for the imaginary part of the tidal response. As a result, the maximum possible rate of change in tidal response, as a function of forcing frequency, is the same as for the homogeneous body. Two frequencies which differ by a factor of 2 will have lag angles which differ by, at most, a factor of two. Whether the larger lag angle is at the higher or lower frequency will depend on proximity to modal peaks.

[56] We know very little, at present, about the viscosity structure within Mars. However, the smaller size of Mars, compared to Earth, and larger surface to volume ratio suggests that the interior of Mars is likely to be cooler and thus more viscous than the Earth, all else being equal. Thermal evolution models of support this notion [*Spohn et al.*, 1998, 2001; *Nimmo and Stevenson*, 2000]. If we take 10^{21} Pa s as a representative viscosity, which is typical of the estimates obtained for global average upper mantle viscosity of Earth [*Peltier*, 1974; *Mitrovica*, 1996], and also assume a rigidity of 10^{11} Pa, as mentioned above, the Maxwell time will be 10^{10} s, or roughly 320 years. In that case, the orbital periods of Phobos and Mars are both very much in the high frequency, elastic response domain. We would thus expect the Love number estimates obtained from solar tidal perturbations on artificial satellite orbits to be quite independent of the forcing frequency. If the effective viscosity of Mars were as low at 10^{18} Pa s, which is characteristic of terrestrial regions with high heat flow, such as the mid-Atlantic ridge at Iceland [*Sjoberg et al.*, 2000], or in continental settings of active tectonic deformation [*Bills et al.*, 1994; *Dixon et al.*, 2004], the Maxwell time would be only 0.3 year, so that some viscous relaxation could occur during the Mars orbital period. However, as noted above, thermal arguments would seem to suggest that the viscosity within Mars should be much higher than that.

[57] Another important influence on the rheology of terrestrial mantle rock is the water content. Recent work has shown that addition of only a few parts per million of water to initially dry olivine, in temperature and pressure environments similar to those in the terrestrial upper mantle, can reduce the viscosity by a factor of 30 [*Hirth and Kohlstedt*, 1996; *Dixon et al.*, 2004]. It seems clear that using terrestrial analogs to predict the viscosity of the mantle of Mars is still rather problematic.

[58] The spatio-temporal pattern associated with viscoelastic tidal deformation combines several effects. For an elastic tide, the deformation is symmetric about the line connecting the center of the deforming body and the tide-raising body. The spatial pattern of deformation is a weighted sum of Legendre polynomials in angular distance from that line, as seen from the center of the deforming body. Viscoelastic deformation differs from the elastic pattern in two important regards. The amplitudes of deformation at each harmonic degree will differ from the elastic values, and the axis of symmetry for each harmonic degree will correspond to a past (rather than current) location of the tide raising body. The time lags will generally be different for different harmonic degrees.

[59] Each harmonic constituent of the tidal potential has a spatial pattern proportional to $P_j[\cos(\gamma)]$ where γ is the angular separation from the symmetry axis of that constituent. Assuming an equatorial orbit for the satellite, we can write this separation angle as a function of the longitude of the tide-raising body ϕ_s and the latitude θ and longitude ϕ of the surface point as

$$\cos\gamma = \cos\theta\cos(\Delta\phi), \tag{36}$$

where the longitude difference is abbreviated

$$\Delta\phi = \phi_s - \phi. \tag{37}$$

If the angular rates are σ for rotation of the deforming body, and n for orbital motion of the tide raising body, then the rate of change of the longitude difference is

$$\frac{d\,\Delta\phi}{dt} = n - \sigma = q. \tag{38}$$

The three bodies for which tidal motions are of interest at Mars are the Sun, Phobos, and Deimos. As the sidereal rotation rate of Mars is

$$\sigma = 350.892^\circ/\mathrm{d}, \tag{39}$$

the corresponding tidal rates and fundamental periods are given in Table 5.

[60] We now reformulate the tidal evolution model of *Redmond and Fish* [1964] incorporating the behavior of a homogeneous Maxwell rheology. It should be noted that we are not suggesting that Mars is actually homogeneous. Rather, we are attempting to test the hypothesis that we can find a simple mechanical model which approximates the behavior which is observed. It is convenient to rewrite the Legendre polynomials in the tidal potential function in terms of the explicit locations of the tide raising body and

the point at which the potential is evaluated, and then evaluate them on the equator. This yields

$$P_2[\cos\gamma] = c_{2,0} + c_{2,2}\cos 2\Delta\phi = (1 + 3\cos 2\Delta\phi)/4, \quad (40)$$

$$P_3[\cos\gamma] = c_{3,1}\cos\Delta\phi + c_{3,3}\cos 3\Delta\phi = (3\cos\Delta\phi + 5\cos 3\Delta\phi)/8, \quad (41)$$

$$P_4[\cos\gamma] = c_{4,0} + c_{4,2}\cos 2\Delta\phi + c_{4,4}\cos 4\Delta\phi = (9 + 20\cos 2\Delta\phi + 35\cos 4\Delta\phi)/64. \quad (42)$$

Thus each harmonic degree will yield several forcing frequencies, each of them an integer multiple of the fundamental synodic frequency for that body.

[61] The induced tidal potential at longitude ϕ, when the tide raising body is at longitude ϕ_s, is

$$\Psi(\phi_s, \phi) = m_s \sum_j \left(\frac{R}{a}\right)^{2j+1} \sum_{h=0}^{j} |k_j(h\ q)| \cdot c_{j,h}\cos(h\ (\phi - \phi_s - \chi(h\ q)), \quad (43)$$

where χ is the phase lag between imposed and induced potential. The tidal torque is the product of a tidal force and a corresponding lever arm. The acceleration is obtained as the derivative of the induced potential with respect to position of the tide raising body, evaluated at the location of the satellite itself. Equating the rate of change of orbital angular momentum to the applied tidal torque, we now obtain the viscoelastic version of the tidal evolution equation

$$\frac{1}{n}\frac{dn}{dt} = -3n\frac{m_s}{m_p}\sum_j \left(\frac{R}{a}\right)^{2j+1} \sum_{h=0}^{j} |k_j(h\ q)|\ c_{j,h}\ h\sin(h\ \chi(h\ q)). \quad (44)$$

This is equivalent to equation (13), but with more explicit forms for the Love number and phase lag. We note that, at a given forcing frequency, there is generally only little variation in phase lag with changing harmonic degree. However, the spectral decomposition of the Legendre polynomials (in equations (40), (41), and (42)) clearly indicates that there are widely differing forcing frequencies associated with the different harmonics. Thus the assumption of a common phase lag for all the tidal constituents, as was done in the preceding section, is seen to be a rather poor approximation.

[62] If we use a homogeneous Maxwell model, there are only two unknown parameters: the effective rigidity μ and the effective viscosity η. We have 3 observational constraints on the frequency dependent viscoelastic Love number of Mars. The first constraint comes from the values discussed above for the degree two Love number, which are estimates of the absolute value of that parameter at the semidiurnal solar synodic period. The functional form of the constraint is given in equation (35). The second and third constraints come from the estimates of the secular acceleration rates of Phobos and Deimos, which yield weighted sums of the complex Love numbers at multiples of their respective synodic periods. The functional forms of those constraints are given in equation (44), immediately above. Ideally, we should be able to estimate the Mars mechanical parameters from any two of the three observations, or obtain a weighted least-squares estimate from all three constraints. What we find is that the least-squares solution

$$\mu = (4.6 \pm 2.0) \times 10^{10}\ \text{Pa}$$

$$\eta = (8.7 \pm 0.6) \times 10^{14}\ \text{Pa s}$$

is virtually identical to the two-parameter solution obtained using the solar-forced Love number and Phobos secular acceleration alone.

[63] In contrast to the situation for Phobos, neither of the two constraint pairs involving Deimos yields a valid solution. The value predicted for the Deimos secular acceleration rate, using the estimated Mars interior parameters is -3.1×10^{-7}deg/yr^2, which is roughly 10% of the estimates by *Jones et al.* [1989] and *Sinclair* [1989], but only about 2% of the estimate of *Jacobson et al.* [1989]. It thus appears that the existing estimates of secular acceleration for Deimos are still too large. Of course, it could be that our model is too simple, and a homogeneous Maxwell model does not properly capture the tidal dissipation behavior of Mars.

[64] We note, for comparison, that using Earth values of $k_2 = 0.302$ and a phase lag of 0.20° for the lunar semidiurnal tide [*Ray et al.*, 2001], the effective rigidity and viscosity values for a homogeneous Maxwell model are

$$\mu = 1.44 \times 10^{11}\ \text{Pa}$$

$$\eta = 2.21 \times 10^{17}\ \text{Pa s}.$$

This rigidity estimate is fairly typical of the terrestrial upper mantle, but the viscosity is quite low compared to published estimates of terrestrial mantle values [*Peltier*, 1974; *Mitrovica*, 1996]. In the case of Earth, it is clear that the presence of a substantial fluid core yields a global effective viscosity substantially lower than the mean mantle viscosity. The source of enhanced dissipation within Mars is not obvious.

[65] *Yoder et al.* [2003] argued, from the relatively large size of the degree two Love number, that Mars has a substantial fluid core. While not disputing that as a possible interpretation, we note that our homogeneous Maxwell model equally well satisfies the observed value of the solar forced tidal response of Mars. The fact that the effective viscosity of Mars estimated this way is 250 times less than the estimate derived for Earth suggests that presence of a fluid core is not the entire explanation. As noted above, thermal considerations suggest that, all else being equal, mantle viscosity within Mars should be substantially larger than for Earth. A somewhat more volatile rich mantle for Mars would bring the two values closer together, but still

fails to explain why Mars should be less viscous than Earth. One attractive mechanism for producing large amounts of dissipation is tidally forced flow of a fluid within a porous solid [*Nield et al.*, 2004]. In the present context that could involve water in near-surface rock layers [*Clifford*, 1993; *Clifford and Parker*, 2001], or partial melt within the mantle [*Kiefer*, 2003; *Wenzel et al.*, 2004].

4.4. Orbital Evolution

[66] We now consider the longer term implications of the tidal evolution of the orbit of Phobos. Kepler's third law of planetary motion relates the size of an orbit to the orbital period, and can be written as

$$a^3 n^2 = M^2 = G(m_p + m_s), \tag{45}$$

where a is the orbital semimajor axis, G is the gravitational constant, and (m_p, m_s) are the masses of the orbiting bodies. Upon differentiation, this yields a relationship between the observed secular increase in mean motion and a corresponding secular decrease in semimajor axis. The implied rate is

$$\frac{da}{dt} = -\frac{2}{3}\frac{a}{n}\frac{dn}{dt} = -\frac{4}{3}\frac{a\ s}{n} = (-4.03 \pm 0.03)\text{cm/yr}. \tag{46}$$

Note that we have followed the usual convention of estimating the coefficient s of the quadratic term in mean longitude, rather than the linear term in the rate of mean motion change, so that

$$\frac{dn}{dt} = 2\ s. \tag{47}$$

The orbit of Phobos is shrinking at rate similar to that at which the lunar orbit is growing. A linear extrapolation of this rate would suggest a remaining lifetime for Phobos of ~150 million years, at which point it would impact onto the surface of Mars. However, as will be discussed below, the orbital evolution is quite nonlinear, and the expected demise of Phobos will be rather sooner than the linear estimate would suggest.

[67] The total energy (kinetic plus potential) in a binary orbit is

$$E = -\frac{G\ m_p\ m_s}{2a}, \tag{48}$$

where G is the gravitational constant, and (m_p, m_s) are the masses of the orbiting bodies. The rate of orbital energy loss for Phobos is

$$\frac{dE}{dt} = -\frac{E}{a}\frac{da}{dt} = -(3.35 \pm 0.01) \times 10^6\ \text{W}. \tag{49}$$

[68] It is instructive to write the tidal evolution formula of *Redmond and Fish* [1964] entirely in terms of the semimajor axis, rather than the mean motion. The result is

$$\frac{1}{a}\frac{da}{dt} = 2\beta\ a^{-3/2} \sum_{j=2} k_j\ F_j(\gamma) \left(\frac{R}{a}\right)^{2j+1}, \tag{50}$$

where we have combined the mass dependent terms in the single parameter

$$\beta = \alpha M = \frac{m_s}{m_p}\sqrt{G(m_p + m_s)} = (0.10907 \pm 0.00028)\ \text{m}^{3/2}\ \text{s}^{-1}. \tag{51}$$

If the orbital evolution were dominated by the degree 2 tide, we could write

$$\frac{da}{dt} = -f_2\ a^{-11/2}, \tag{52}$$

with

$$f_2 = 4\beta\ \gamma\ k_2\ R^5. \tag{53}$$

The solution to this differential equation, assuming f_2 to be constant, is

$$a[t] = \left(a[0] - \frac{13}{2} f_2\ t\right)^{2/13}. \tag{54}$$

This solution was used by *Burns* [1978] to estimate a remaining lifetime for Phobos of 30–50 million years. We note, however, that this is best viewed as an upper bound, since the effect of higher degree harmonic tides increases rapidly as Phobos gets closer to Mars. Our estimates of the tidal Love numbers suggest that 10% of the present secular acceleration is due to harmonic degree 3, and that ratio increases with a^{-2}. During the late stages of orbital evolution, the rate of orbital decay will be appreciably higher than would be estimated from the degree two contribution alone. A more accurate assessment of the final stages of the orbital evolution of Phobos would take into account the dependence of the phase lags on the forcing period, as was discussed above in connection with a viscoelastic response model.

[69] Of course, the latest stages of orbital evolution will presumably involve a tidally disrupted cloud of small particles. Phobos is already inside the classical Roche limit, at which a fluid would be pulled apart. The role of finite strength complicates the analysis considerably, and it is difficult to predict when Phobos will disintegrate [*Dobrovolskis*, 1982, 1990; *Bottke et al.*, 1997; *Davidsson*, 1999; *Holsapple*, 2001]. The story beyond that point would involve formation and evolution of an ephemeral ring system [*Bills*, 1992; *Colwell*, 1994].

5. Summary

[70] We report on new observations of the orbital position of Phobos, which require an adjustment to previous estimates of secular acceleration in longitude. Our new estimate for that parameter is slightly higher, and much better constrained, than the several estimates which were published circa 1990. The significant improvement in the accuracy of determination arises from a combination of accurate measurements and extended time span of observations. The rate of secular acceleration in longitude directly determines the rate at which orbital energy is being dissi-

pated. Our analyses of the tidal lag angle, and attempts to constrain internal dissipation mechanisms within Mars, are more limited, since they require knowledge of other parameters, some of which are still rather uncertain. Continued observations of Phobos and Deimos will eventually allow improved estimates of the tidal response of Mars, which will yield constraints on the mechanical properties of the deep interior.

References

Abshire, J. B., X. Sun, and R. S. Afzal (2000), Mars Orbiter Laser Altimeter: Receiver model and performance analysis, *Appl. Opt.*, *39*, 2440–2460.

Acton, C. H. (1996), Ancillary data services of NASA's navigation and ancillary information facility, *Planet Space Sci.*, *44*, 65–70.

Aksnes, K., and F. A. Franklin (2001), Secular acceleration of Io from mutual satellite events, *Astron. J.*, *122*, 2734–2739.

Allison, M., and M. McEwen (2000), A post-Pathfinder evaluation of areocentric solar coordinates with improved timing recipes for Mars seasonal/diurnal climate studies, *Planet. Space Sci.*, *48*, 215–235.

Alterman, Z., H. Jarosch, and C. L. Pekeris (1959), Oscillations of the Earth, *Proc. R. Soc. London, Ser. A*, *252*, 80–95.

Avensov, G. A., et al. (1989), Television observations of Phobos, *Nature*, *341*, 585–587.

Banerdt, W. B., and G. A. Neumann (1999), The topography and ephemeris of Phobos from MOLA ranging, *Lunar Planet. Sci.*, *XXX*, abstract 2021.

Bell, J. F., et al. (2004a), Pancam multispectral imaging results from the Spirit Rover at Gusev crater, *Science*, *305*, 800–806.

Bell, J. F., et al. (2004b), Pancam multispectral imaging results from the Opportunity Rover at Meridiani Planum, *Science*, *306*, 1703–1709.

Bills, B. G. (1992), Venus satellite orbital decay, ephemeral ring formation, and subsequent crater production, *Geophys. Res. Lett.*, *19*, 1025–1028.

Bills, B. G., and R. L. Comstock (2005), Spatial and temporal patterns of solar eclipses by Phobos on Mars, *J. Geophys. Res.*, *110*, E04004, doi:10.1029/2003JE002209.

Bills, B. G., D. R. Currey, and G. A. Marshall (1994), Viscosity estimates for the crust and upper mantle from patterns of lacustrine shoreline deformation in the eastern Great Basin, *J. Geophys. Res.*, *99*, 22,059–22,086.

Bottke, W. F., D. C. Richardson, and S. G. Love (1997), Can tidal disruption of asteroids make crater chains on the Earth and Moon?, *Icarus*, *126*, 470–474.

Burns, J. A. (1972), The dynamical characteristics of Phobos and Deimos, *Rev. Geophys.*, *10*, 462–483.

Burns, J. A. (1978), The dynamical evolution and origin of the Martian moons, *Vistas Astron.*, *22*, 193–210.

Burns, J. A. (1992), Contradictory clues as to the origin of the Martian moons, in *Mars*, pp. 1283–1302, Univ. of Ariz. Press, Tucson.

Cazenave, A., A. Dobrovolskis, and B. Lago (1980), Orbital history of the Martian satellites with inferences on their origin, *Icarus*, *44*, 730–744.

Christou, A. A. (2002), Lander position determination on Mars using Phobos transits: Application to Beagle 2, *Planet Space Sci.*, *50*, 781–788.

Clifford, S. M. (1993), A model for the hydrologic and climatic behavior of water on Mars, *J. Geophys. Res.*, *98*, 10,973–11,016.

Clifford, S. M., and T. J. Parker (2001), The evolution of the Martian hydrosphere: Implications for the fate of a primordial ocean and the current state of the northern plains, *Icarus*, *154*, 40–79.

Colwell, J. E. (1994), The disruption of planetary satellites and the creation of planetary rings, *Planet. Space Sci.*, *42*, 1139–1149.

Darwin, G. H. (1911), *The Tides and Kindred Phenomena in the Solar System*, 437 pp., John Murray, London.

Davidsson, B. J. R. (1999), Tidal splitting and rotational breakup of solid spheres, *Icarus*, *142*, 525–535.

Dickey, J. O., et al. (1994), Lunar laser ranging: A continuing legacy of the Apollo program, *Science*, *265*, 482–490.

Dixon, J. E., T. H. Dixon, D. R. Bell, and R. Malservisi (2004), Lateral variation in upper mantle viscosity: Role of water, *Earth Planet. Sci. Lett.*, *222*, 451–467.

Dobrovolskis, A. R. (1982), Internal stresses in Phobos and other triaxial bodies, *Icarus*, *52*, 136–148.

Dobrovolskis, A. R. (1990), Tidal disruption of solid bodies, *Icarus*, *88*, 24–38.

Duxbury, T. C. (1978), Spacecraft imaging of Phobos and Deimos, *Vistas Astron.*, *22*, 149–161.

Dziewonski, A. M., and D. L. Anderson (1981), Preliminary reference Earth model, *Phys. Earth Planet. Inter.*, *25*, 297–356.

Egbert, G. D., and R. D. Ray (2003), Semi-diurnal and diurnal tidal dissipation from TOPEX/Poseidon altimetry, *Geophys. Res. Lett.*, *30*(17), 1907, doi:10.1029/2003GL017676.

Fischer, H. J., and T. Spohn (1990), Thermal orbital histories of viscoelastic models of Io, *Icarus*, *83*, 39–65.

Folkner, W. M., C. F. Yoder, D. N. Yuan, E. M. Standish, and R. A. Preston (1997), Interior structure and seasonal mass redistribution of Mars from radio tracking of Mars Pathfinder, *Science*, *278*, 1749–1752.

Goldreich, P., and P. D. Nicholson (1977), Turbulent viscosity and Jupiter's tidal Q, *Icarus*, *30*, 301–304.

Hall, A. (1878), Observations and orbits of the satellites of Mars with data for ephemerides in 1879, U.S. Govt. Print. Off., Washington, D. C.

Hamilton, D. P. (1996), The asymmetric time-variable rings of Mars, *Icarus*, *119*, 153–172.

Hestroffer, D., and C. Magnan (1998), Wavelength depencency of the solar limb darkening, *Astron. Astrophys.*, *333*, 338–342.

Hirth, G., and D. L. Kohlstedt (1996), Water in the oceanic upper mantle: Implications for rheology, melt extraction and the evolution of the lithosphere, *Earth Planet. Sci. Lett.*, *144*, 93–108.

Holsapple, K. A. (2001), Equilibrium configurations of solid cohesionless bodies, *Icarus*, *154*, 432–448.

Howard, J. E., A. V. Krivov, and F. Spahn (2003), Transverse halo orbits about Mars?, *Geophys. Res. Lett.*, *30*(13), 1680, doi:10.1029/2003GL017677.

Hussman, H., and T. Spohn (2004), Thermal-orbital evolution of Io and Europa, *Icarus*, *171*, 391–410.

Ioannou, P. J., and R. S. Lindzen (1993), Gravitational tides in the outer planets, *Astrophys. J.*, *406*, 266–278.

Jacobson, R. A., S. P. Synnott, and J. K. Campbell (1989), The orbits of the satellites of Mars from spacecraft and Earthbased observations, *Astron. Astrophys.*, *225*, 548–554.

Jones, D. H. P., A. T. Sinclair, and I. P. Williams (1989), Secular acceleration of Phobos confirmed from positions obtained on La Palma, *Mon. Not. R. Astron. Soc.*, *237*, 15–19.

Kiefer, W. S. (2003), Melting in the martian mantle: Shergottite formation and implications for present-day mantle convection on Mars, *Meteorit. Planet. Sci.*, *38*, 1815–1832.

Lambeck, K. (1979), On the orbital evolution of the Martian satellites, *J. Geophys. Res.*, *84*, 5651–5658.

Lemoine, F. G., D. E. Smith, D. D. Rowlands, M. T. Zuber, G. A. Neumann, D. S. Chinn, and D. E. Pavlis (2001), An improved solution of the gravity field of Mars (GMM-2B) from Mars Global Surveyor, *J. Geophys. Res.*, *106*, 23,359–23,376.

Lieske, J. H. (1987), Galilean satellite evolution: Observational evidence for secular changes in mean motions, *Astron. Astrophys.*, *176*, 146–158.

Lopes-Gautier, R., et al. (1999), Active volcanism on Io: Global distribution and variations in activity, *Icarus*, *140*, 243–264.

Love, A. E. H. (1911), *Some Problems of Geodynamics*, Cambridge Univ. Press, New York.

Mignard, F. (1981), Evolution of the Martian satellites, *Mon. Not. R. Astron. Soc.*, *194*, 365–379.

Mitrovica, J. X. (1996), Haskell [1935] revisited, *J. Geophys. Res.*, *101*, 555–569.

Mordovskaya, V. G., N. N. Oraevksy, and J. Rustenbach (2001), Interaction of Phobos with the solar wind plasma, *Cosmic. Res.*, *39*, 446–452.

Morley, T. A. (1989), A catalogue of ground-based astrometric observations of the Martian satellites, 1877–1982, *Astron. Astrophys. Suppl. Ser.*, *77*, 209–226.

Munk, W., and G. J. F. MacDonald (1960), *The Rotation of the Earth: A Geophysical Discussion*, Cambridge Univ. Press, New York.

Nazzario, R. C., and T. W. Hyde (1997), The dust bands of the planet Mars, *Adv. Space Res.*, *20*, 1535–1538.

Neumann, G. A., D. D. Rowlands, F. G. Lemoine, D. E. Smith, and M. T. Zuber (2001), Crossover analysis of Mars Orbiter Laser Altimeter data, *J. Geophys. Res.*, *106*, 23,753–23,768.

Nield, D. A., A. V. Kuznetsov, and M. Ziong (2004), Effects of viscous dissipation and flow work on forced convection in a channel filled by a saturated porous medium, *Transp. Porous Media*, *56*, 351–367.

Nimmo, F., and D. J. Stevenson (2000), Influence of early plate tectonics on the thermal evolution and magnetic field of Mars, *J. Geophys. Res.*, *105*, 11,969–11,979.

Patterson, W. R., F. O. Huck, S. D. Wall, and M. R. Wolf (1977), Calibration and performance of the Viking lander cameras, *J. Geophys. Res.*, *82*, 4389–4400.

Peale, S. J. (2003), Tidally induced volcanism, *Celest. Mech. Dyn. Aston.*, *87*, 129–155.

Peale, S. J., and M. H. Lee (2002), A primordial origin of the Laplace relation among the Galilean satellites, *Science*, *298*, 593–597.

Peale, S. J., P. Cassen, and R. T. Reynolds (1979), Melting of Io by tidal dissipation, *Science*, *203*, 892–894.

Peltier, W. R. (1974), Impulse response of a Maxwell Earth, *Rev. Geophys.*, *12*, 649–669.
Ray, R. D., R. J. Eanes, and F. G. Lemoine (2001), Constraints on energy dissipation in the Earth's body tide from satellite tracking and altimetry, *Geophys. J. Int.*, *144*, 471–480.
Redmond, J. C., and F. F. Fish (1964), The luni-tidal interval in Mars and the secular accleration of Phobos, *Icarus*, *3*, 87–91.
Russell, C. T., J. G. Luhmann, K. Schwingenschuh, W. Riedler, and Y. Yeroshenko (1990), Upstream waves at Mars, *Geophys. Res. Lett.*, *17*, 897–900.
Sabadini, R., and W. R. Peltier (1981), Pleistocene deglaciation and the Earth's rotation: Implications for mantle viscosity, *Geophys. J. R. Astron. Soc.*, *66*, 553–578.
Sabadini, R., G. Spada, and Y. Ricard (1993), Time dependent density anomalies in a stratified, viscoelastic mantle: Implications for the geoid, Earth's rotation, and sea-level fluctuations, *Surv. Geophys.*, *14*, 537–553.
Sagdeev, R. Z., and A. V. Zakharov (1989), Brief history of the Phobos mission, *Nature*, *341*, 581–585.
Sauer, K., E. Dubinin, K. Baumgartel, and A. Bogdanov (1995), Deimos—An obstacle to the solar wind, *Science*, *269*, 1075–1078.
Segatz, M., T. Spohn, M. N. Ross, and G. Schubert (1988), Tidal dissipation, surface heat flow, and figure of viscoelastic models of Io, *Icarus*, *75*, 187–206.
Seidelmann, P. K., et al. (2002), Report of the IAU/IAG Working Group on cartographic coordinates and rotational elements of the planets and satellites, *Celest. Mech. Dyn. Astron.*, *82*, 83–110.
Sharpless, B. P. (1945), Secular accelerations in the longitudes of the satellites of Mars, *Astron. J.*, *51*, 185–186.
Sinclair, A. T. (1972), The motions of the satellites of Mars, *Mon. Not. R. Astron. Soc.*, *155*, 249–274.
Sinclair, A. T. (1989), The orbits of the satellites of Mars determined from Earth-based and spacecraft observations, *Astron. Astrophys.*, *220*, 321–328.
Sjoberg, L. E., M. Pan, E. Asenjo, and S. Erlingsson (2000), Glacial rebound near Vatnajokull, Iceland, studied by GPS campaigns in 1992 and 1996, *J. Geodyn.*, *29*, 63–70.
Smith, D. E., M. T. Zuber, R. M. Haberle, D. D. Rowlands, and J. R. Murphy (1999), The Mars seasonal CO_2 cycle and the time variation of the gravity field: A general circulation model simulation, *J. Geophys. Res.*, *104*, 1885–1896.
Smith, D. E., et al. (2001a), Mars Orbiter Laser Altimeter: Experiment summary after the first year of global mapping of Mars, *J. Geophys. Res.*, *106*, 23,689–23,722.
Smith, D. E., M. T. Zuber, and G. A. Neumann (2001b), Seasonal variation of snow depth on Mars, *Science*, *294*, 2141–2146.
Smith, D. E., M. T. Zuber, M. H. Torrence, and P. J. Sunn (2003), Estimating the k_2 tidal gravity Love number of Mars, *Eos Trans. AGU*, *84*(46), Fall Meet. Suppl., Abstract P31A-05.
Smith, J. C., and G. H. Born (1976), Secular acceleration of Phobos and Q of Mars, *Icarus*, *27*, 51–53.
Spohn, T., F. Sohl, and D. Breuer (1998), Mars, *Astron. Astrophys. Rev.*, *8*, 181–235.
Spohn, T., M. H. Acuna, D. Breuer, M. Golombek, R. Greeley, A. Halliday, E. Hauber, R. Jaumann, and F. Sohl (2001), Geophysical constraints on the evolution of Mars, *Space Sci. Rev.*, *96*, 231–262.
Standish, E. M., X. X. Newhall, J. G. Williams, and W. M. Folkner (1995), JPL Planetary and Lunar Ephemerides, DE403/LE403, *JPL Rep. IOM 314.10-127*, Jet Propul. Lab., Pasadena, Calif.
Standish, E. M., X. X. Newhall, J. G. Williams, and W. M. Folkner (2003), JPL Planetary and Lunar Ephemerides, DE410, *JPL Rep. IOM 312.N.03-007*, Jet Propul. Lab., Pasadena, Calif.
Stephenson, F. R., and L. V. Morrison (1995), Long-term fluctuations in the Earth's rotation: 700 BC to AD 1990, *Philos. Trans. R. Soc. London, Ser. A*, *351*, 165–202.
Szeto, A. (1983), Orbital evolution and origin of the Martian satellites, *Icarus*, *55*, 133–168.
Vermeersen, L. L. A., and R. Sabadini (1997), A new class of stratified viscoelastic models by analytical techniques, *Geophys. J. Int.*, *129*, 531–570.
Vermeersen, L. L. A., R. Sabadini, and G. Spada (1996), Compressible rotational deformation, *Geophys. J. Int.*, *126*, 735–761.
Wenzel, M. J., M. Manga, and A. M. Jellinek (2004), Tharsis as a consequence of Mars' dichotomy and layered mantle, *Geophys. Res. Lett.*, *31*, L04702, doi:10.1029/2003GL019306.
Widmer, R., G. Masters, and F. Gilbert (1991), Spherically symmetric attenuation within the Earth from normal mode data, *Geophys. J. Int.*, *104*, 541–553.
Wilhelm, H. (1986), Spheroidal and toroidal stress coefficients, *J. Geophys.*, *59*, 16–22.
Wilson, R. E. (1994), Binary-star light-curve models, *Publ. Astron. Soc. Pac.*, *106*, 921–941.
Woolard, E. W. (1944), The secular perturbations of the satellites of Mars, *Astron. J.*, *51*, 33–36.
Wu, P., and W. R. Peltier (1982), Viscous gravitational relaxation, *Geophys. J. R. Astron. Soc.*, *70*, 435–485.
Yoder, C. (1982), Tidal rigidity of Phobos, *Icarus*, *49*, 327–346.
Yoder, C. F., and S. J. Peale (1981), The tides of Io, *Icarus*, *47*, 1–35.
Yoder, C. F., A. S. Konopliv, D. N. Yuan, E. M. Standish, and W. M. Folkner (2003), Fluid core size of Mars from detection of the solar tide, *Science*, *300*, 299–303.
Yokoyama, T. (2002), Possible effects of secular resonances in Phobos and Triton, *Planet. Space Sci.*, *50*, 63–77.
Yuan, D. N., W. L. Sjogren, A. S. Konopliv, and A. B. Kucinskas (2001), The gravity field of Mars: A 75th degree and order model, *J. Geophys. Res.*, *106*, 23,377–23,401.
Zuber, M. T., D. E. Smith, S. C. Solomon, D. O. Muhleman, J. W. Head, J. B. Garvin, J. B. Abshire, and J. L. Bufton (1992), The Mars Observer Laser Altimeter investigation, *J. Geophys. Res.*, *97*, 7781–7797.

B. G. Bills, Scripps Institution of Oceanography, La Jolla, CA 92093, USA. (bbills@ucsd.edu)
G. A. Neumann and D. E. Smith, NASA Goddard Space Flight Center, Greenbelt, MD 20771, USA.
M. T. Zuber, Massachusetts Institute of Technology, 77 Massachusetts Avenue, Cambridge, MA 02139, USA.